Journal of Alloys and Compounds 681 (2016) 486–491

Contents lists available at ScienceDirect

Journal of Alloys and Compounds

journal homepage: http://www.elsevier.com/locate/jalcom

Facile solution synthesis of tin sulfide nanobelts for lithium-ion batteries

Keyu Li [a], Shancheng Yan [a, *], Zixia Lin [b], Yi Shi [c, **]

[a] School of Geography and Biological Information, Nanjing University of Posts and Telecommunications, Nanjing 210023, PR China
[b] National Laboratory of Solid State Microstructures, Nanjing University, Nanjing 210093, PR China
[c] Collaborative Innovation Center of Advanced Microstructures, Nanjing University, Nanjing 210093, PR China

ARTICLE INFO

Article history:
Received 31 December 2015
Received in revised form
25 April 2016
Accepted 26 April 2016
Available online 27 April 2016

Keywords:
SnS nanobelts
Hydrothermal approach
Anode materials
Lithium-ion batteries
High reversible capacity

ABSTRACT

Two-dimensional Sn-based metal compounds (e.g. SnS, SnS_2 and SnO_2) are exceptionally attractive due to their excellent ion intercalation response and are suitable for use in energy storage devices (e.g. lithium-ion batteries and supercapacitors). However, the application of these dichalcogenides in Li-ion batteries is hindered by limitations in large-scale solution synthesis of SnS nanobelts. In this study, we developed a universal hydrothermal approach for the synthesis of SnS nanobelts and proposed an underlying mechanism for the formation reaction. When used as anode materials for lithium-ion batteries, SnS nanobelts maintain a discharge capacity of 889.9 $mAhg^{-1}$ after 50 cycles at a current density of 0.1 A/g. The nanobelts also exhibit high electrochemical performance, high rate capacity, and high reversible capacity. These results demonstrate that SnS nanobelts are potential anode materials for high-performance energy storage applications.

1. Introduction

Sn-based materials have gained considerable attention as future-generation Lithium-ion batteries (LIBs) due to their low cost, high theoretical capacity and large number of potential applications that hinges upon the electrical properties [1–9]. Amongst such materials, SnS possesses an orthorhombic structure, where tightly bound Sn–S atoms are connected by the van der Waals forces [10,11]. The crystallographic feature can facilitate Li^+ diffusion, and functions as the buffering layer to compensate for large volume changes [12]. Moreover, SnS is low-cost, nontoxic, abundant and heavy metal-free [11]. With its high specific capacity, low cost, nontoxicity, and high electrical conductivity, SnS is a promising material for various applications, such as in LIBs, field-emission applications, photodetector devices, photocatalysts, and optoelectronics [11,13–21]. SnS with various nanostructures have been successfully synthesized through different methods [11–19,22–24]. Nevertheless, the following issues are still inevitable: 1) synthesis is complicated and mostly requires the use of hexamethyldisilazane and annealing treatment under high temperature in N_2 gas; [5,12]; 2) limited control of SnS phase and morphology [11,14,18,23]; 3) and poor electrochemical properties due to excessive volume expansion during cycling [25]. The electrochemical reaction mechanism between SnS and lithium ions is generally proposed as follows [12,14,26,27]:

$$SnS(s) + 2Li^+ + 2e^- \rightarrow Sn(s) + Li_2S(s) \quad (1)$$

$$Sn(s) + 4.4Li^+ + 4.4e \rightleftharpoons Li_{4.4}Sn(s) \quad (2)$$

The first-step of the reaction has generally been considered to be irreversible and the theoretical capacity of SnS is calculated to be 782 $mAhg^{-1}$ (4.4Li/Sn) based only on the second step. It should be noted that the theoretical capacity of SnS based on the theoretical maximum (6.4Li/Sn) is 1138 $mAhg^{-1}$ if Li_2S can be decomposed completely according to the reversible reaction ($SnS + 6.4Li^+ + 6.4e^- \leftrightarrow Li_{4.4}Sn + Li_2S$) [28–31]. Recent reports have also suggested that SnS_2 can realize a reversible conversion (formation and decomposition of Li_2S) via a probable novel mechanism for the storage of Li^+ [29,30]. Therefore, it will be a significant challenge to explore a simple, environmentally friendly, controllable and rational synthesis design for SnS with high reversible capacity.

In this study, SnS nanobelts were synthesized via a simple,

* Corresponding author.
** Corresponding author.
E-mail address: yansc@njupt.edu.cn (S. Yan).

http://dx.doi.org/10.1016/j.jallcom.2016.04.280
0925-8388/

facile, and controllable hydrothermal route by controlling the change in solution color and state during the mixing stage, which allows the realization of controllable morphology for the final products. Contrary to previous reports, it has been found that the Tin source for the transformation of valence state for high reversible capacity is Sn^{4+} instead of Sn^{2+} When applied to electrochemical tests as a potential anode for LIBs, SnS nanobelts maintained a discharge capacity of 889.9 $mAhg^{-1}$ after 50 cycles at a current density of 0.1 A/g. SnS nanobelt anode also delivers a charge capacity of 890.3 $mAhg^{-1}$ after 50 cycles reversibly and retrieves 5 Li^+ per Sn atom, corresponding to the reversibility of the conversion reaction ($Sn + Li_2S \rightarrow SnS + 2Li^+ + 2e^-$); as high as 30% of Li_2S can be decomposed according to the reversible reaction [28–30]. Hence, these materials exhibit good electronic connectivity, high charge/discharge capacity, and stable cycle performance.

2. Experimental details

2.1. Preparation of SnS nanobelts

In the typical experiment, 1 mmol $SnCl_4 \cdot 5H_2O$ and 2.5 mmol $Na_2S \cdot 9H_2O$ are dissolved in 30 ml of ethylene glycol by magnetic stirring to form a yellow solution. The mixture is placed into a 50 ml Teflon-lined autoclave that is maintained in an oven at 180 °C for 24 h. After cooling to room temperature, the black precipitates are collected from the solution through centrifugal filtration, washed several times using distilled water to remove the organic residues, and dried at 60 °C for 4 h. As a comparison, the same experiment is conducted using $SnCl_2 \cdot 2H_2O$ as a replacement for $SnCl_4 \cdot 5H_2O$.

2.2. Materials characterizations

Field emission scanning electron microscopy (FE-SEM; JSM-7000F) was used to determine the morphology of the samples. Transmission electron microscopy (TEM) and high-resolution transmission electron microscopy (HRTEM) images were obtained using a JEOL model JEM2100 instrument at an accelerating voltage of 200 kV. The crystal phase properties of the samples were analyzed with a Bruker D8 Advance X-ray diffractometer (XRD) using Ni-filtered Cu Kα radiation at 40 kV and 40 mA at 2θ ranging from 10° to 90° with a scan rate of 0.02° per second. An FTIR spectrum was carried on NEXUS870 spectrometer from 2000 cm^{-1}–200 cm^{-1}. Raman spectra were obtained on a Raman spectrometer (JY T64000) excited by the 514.5 nm line of an Ar+ laser under 100 μW. X-ray photoelectron spectroscopy (XPS) analysis (PHI5000 Versaprobe) was used to determine the chemical composition of the products.

2.3. Electrochemical measurements

For lithium ion battery measurements, slurry of active material was prepared with carbon black and polyvinylidene fluoride (PVDF) in a weight ratio of 8:1:1, to form homogeneous slurry in N-methylpyrrolidone (NMP). This was then deposited as a film of thickness 50 μm on a copper foil and dried in vacuum at 80 °C for 12 h. The electrodes were pressed to enhance the contact between the active materials and the conductive carbon. Coin cell assembly was done at room temperature in a glove box under argon. The mass loading of the active material on the working anode electrode was about 0.108 mg. Cyclic voltammograms and galvanostatic charge/discharge cycling were performed at current rates (0.1 A/g) in the voltage range of 0.1 and 1.2 V (versus Li^+/Li). The discharge capacity of SnS electrodes were performed at current density of 0.1, 0.2, 0.4 and 0.8 Ag^{-1}. The first five cyclic voltammograms (CV) over a voltage range of 0.01–3.00 V at a scanning rate of 0.1 mV/s. Electrochemical impedance spectroscopy (EIS) of the fresh cell and after-cycling electrodes obtained by applying a sine wave with an amplitude of 5.0 mV over the frequency range of 1000 kHz–0.01 Hz.

3. Results and discussion

To study the microsphere structure of samples prepared at 180 °C for 24 h, we performed field-emission scanning electron microscopy (FESEM) analysis (Fig. 1a). The morphology of the prepared SnS comprises a large number of nanobelts with lengths of up to several microns. The nanobelt structures may allow the compensation of volume changes and improve cycling performance and stability during Li^+ insertion and deinsertion. The structural and morphological features were investigated by TEM (Fig. 1b). SnS nanobelts are about 150 nm wide. Parallel fringes appear in the HRTEM image (Fig. 1c) and are indicated by the red circle (Fig. 1b). These fringes have a typical spacing of 0.21 nm and are assigned to the (102) lattice planes of the orthorhombic SnS structure. Based on the selected area electron diffraction (SAED) patterns (Fig. 1d), SnS nanoribbons exhibit a single crystalline structure [16,19]. The three characteristic diffraction peaks of (011), (1-11) and (102) belonging to the same zone axis are shown in Fig. 1d, as denoted by white letter; this finding is consistent with the XRD patterns shown in Fig. 2d (red) [32].

X-ray photoelectron spectroscopy (XPS) analysis was performed to investigate the surface chemical composition of the prepared samples. The binding of specimen charging is corrected by referencing C 1s to 284.60 eV. As shown in Fig. 2a, no other peaks of elements other than Sn, S, O, and C were observed. The presence of two strong peaks at 494.85 and 486.35 eV corresponds to the two binding energies of $Sn^{2+}3d_{3/2}$ and $Sn^{2+}3d_{5/2}$, respectively, because of the spin-orbit interaction in the metal sulfide (Fig. 2b). The spacing between the two peaks is about 8.50 eV, which indicates the energy gap between $Sn3d_{5/2}$ and $Sn3d_{3/2}$. The S 2p spectrum shows S 2p at about 161.475 eV (Fig. 2c). This result is consistent with previous reports on SnS [13,14].

It is interesting that the color and state of the solution color change with the transformation of valence state ($Sn^{4+} \rightarrow Sn^{2+} \rightarrow Sn^{4+}$) when the Tin source is Sn^{4+} instead of Sn^{2+} during different solution mixed phases. To explore the evolution of the morphology, the study is conducted by controlling the solution with mixed color and state. The XRD patterns show that the structures of the sample differ at different stages (Fig. 2d). The diffraction of hexagonal SnS_2 corresponds to stages 1 (light yellow transparent liquid) and 3 (yellow turbid solution) (JCPDS 23-0667), and the standard diffraction of the orthorhombic SnS corresponds to stage 2 (yellow solution) (JCPDS 65-3812) [12,25,33]. The XRD pattern of the typical sample with stage 2 (yellow solution) is shown by the red line. Six strong characteristic diffraction peaks of (111), (400), (011), (201), (210), and (311) are indexed to the standard diffraction data of the orthorhombic SnS (JCPDS 65-3812) [12,13,32]. No peak is attributed to SnS_2 in the prepared samples, indicating the highly pure orthorhombic phase of SnS. The sharp and strong peaks also indicate that the as-synthesized SnS products are well-crystallized. These results reveal that the differences between morphology and product composition are affected by mixing stages with changes in color and state.

In the experiment, the solution mixing stage has vital influences on the phase change and the properties of the final product. As shown in Fig. 3a, changes in color and state are detected as light yellow transparent liquid, yellow solution and yellow turbid solution (first-line). Changes in color and state are evident in the solution. To explore the influence of the mixing stage on the

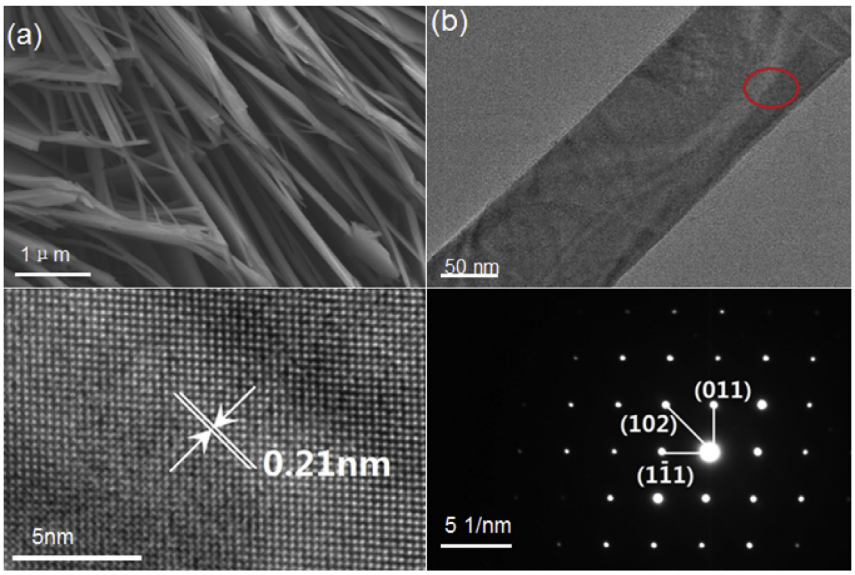

Fig. 1. (a) SEM of SnS nanobelts synthesized at 24 h. (b) TEM of SnS nanobelts. (c) HRTEM image within the red circle from an individual nanobelt in Fig. 1b. (d) SAED pattern. (For interpretation of the references to color in this figure legend, the reader is referred to the web version of this article.)

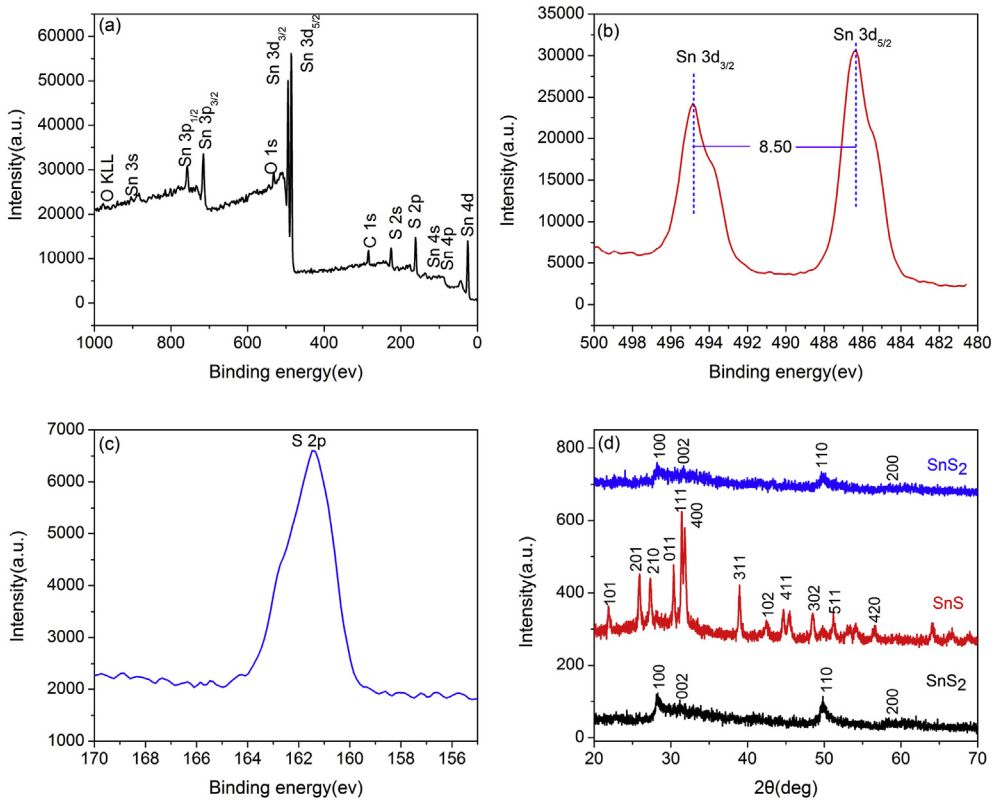

Fig. 2. (a) Full XPS spectrum of the SnS nanobelts synthesized with at 24 h; (b, and c) high-resolution XPS spectra of the SnS nanobelts in the Sn 3d, and S 2p; (d) XRD pattern of sample 1 SnS_2 (black); XRD pattern of sample 2 SnS (red); XRD pattern of sample 3 SnS_2 (blue). (For interpretation of the references to color in this figure legend, the reader is referred to the web version of this article.)

morphology of the sample, we evaluated the final products from different mixing stages (Fig. 3a). The only color observed in stage 2 is black in the red areas. The product of stage 2 is SnS, as shown in the XRD analysis. The products of stages 1 and 3 are colored brown (second-lines 1 and 3). The SEM images of the products obtained at different mixing stages were analyzed to study the morphologies of the specimens. In the first stage, a cluster of nanosheets are clearly observed (third-line 1). The nanosheets grow into nanobelts at stage 2 of mixing (third-line 2) and then reverted back into nanosheets with further mixing (third-line 3).

We performed three controllable experiments at different mixing stages by controlling changes in color and state in solutions

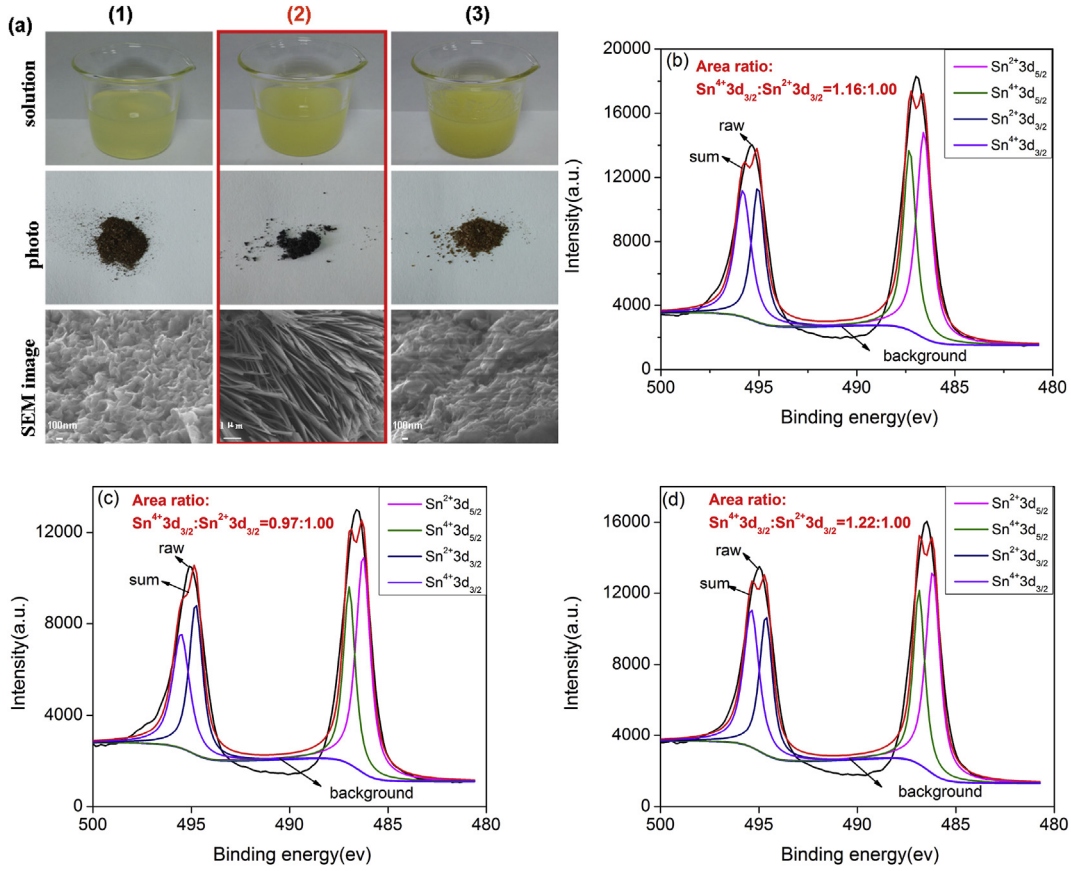

Fig. 3. (a) Three solution states of different mixing stages and SEM images; (b) XPS spectrum of curve fitting and splitting peaks from solution 1; (c) XPS spectrum of curve fitting and splitting peaks from solution 2; (d) XPS spectrum of curve fitting and splitting peaks from solution 3.

1, 2, and 3 (Fig. 3) before testing of lithium storage properties to elucidate the possible formation process of the SnS products. Fig. 3 shows the XPS spectrum of the curve fitting and splitting peaks of $Sn^{4+}3d$ and $Sn^{2+}3d$, which reveals the presence of Sn^{4+} and Sn^{2+} in the same mixing stage. Parameters are adjusted at around 485.92, 487.58, 494.38, and 495.82 eV, which correspond to the four binding energies of $Sn^{2+}3d_{5/2}$, $Sn^{4+}3d_{5/2}$, $Sn^{2+}3d_{3/2}$, and $Sn^{4+}3d_{3/2}$, respectively, to determine the major element present in each stage [13]. The curve fitting results after parameter adjustments are shown in Fig. 3. We only describe the area ratio of the splitting peaks of $Sn^{2+}3d_{3/2}$ and $Sn^{4+}3d_{3/2}$ because those from $Sn^{2+}3d_{5/2}$ and $Sn^{4+}3d_{5/2}$ did not change. Moreover, the binding energy of $Sn3d_{3/2}$ is larger than $Sn3d_{5/2}$ and is not suitable in the analysis of the curve fitting results. As shown in Fig. 3, the area ratios of splitting peaks from $Sn^{4+}3d_{3/2}$:$Sn^{2+}3d_{3/2}$ are 1.16:1.00 (Fig. 3b) and 1.22:1.00 (Fig. 3d), which indicates that the major element in solutions 1 and 3 is Sn^{4+}. By contrast, Sn^{2+} are the major element in solution 2 because the area ratio of splitting peaks from $Sn^{4+}3d_{3/2}$:$Sn^{2+}3d_{3/2}$ are 0.97:1.00 (Fig. 3c). Solution mixing stage affects the morphology of the synthesized products.

Different chemical reactions are likely to occur in solution under the mixed processes of the three stages. A possible novel growth mechanism of SnS is proposed based on experimental results as follows:

$$SnCl_4 \cdot 5H_2O + 2Na_2S \cdot 9H_2O = SnS_2 + 4NaCl + 23H_2O \quad (3)$$

$$Na_2S + 2H_2O = H_2S + 2NaOH \quad (4)$$

$$H_2S \rightleftharpoons HS^- + H^+ \quad (5)$$

$$SnS_2 + Na_2S = Na_2SnS_3 \quad (6)$$

$$SnS_3^{2-} + 2H^+ = H_2S + SnS + S \quad (7)$$

$$(X - 1)\,S + Na_2S = Na_2S_X\ (x = 2–5) \quad (8)$$

$$SnS + Na_2S_2 = SnS_2 + Na_2S \quad (9)$$

The reaction involves two stages. In the first reduction stage, $SnCl_4 \cdot 5H_2O$ quickly reacts with $Na_2S \cdot 9H_2O$ in ethylene glycol to produce SnS_2 (3). SnS is formed through SnS_2 reduction after four reaction steps (4–7). In the second oxidation stage, S reacts with Na_2S to produce Na_2S_2 (x = 2), and SnS_2 is formed through SnS oxidation by Na_2S_2 (8–9).

To study the influence of the Tin source, we conducted a control experiment and replaced $SnCl_4 \cdot 5H_2O$ with $SnCl_2 \cdot 2H_2O$. When $SnCl_2 \cdot 2H_2O$ is selected as the Tin source, the product is inhomogenous nanoribbons (Fig. S1). Furthermore, the phase purity of the synthesized sample was determined through XRD analysis (Fig. S1b). The two strong peaks at 2θ values of 31.46° and 31.94° are attributed to the typical peaks of (111) and (400), respectively, of the orthorhombic SnS (JCPDS 65-3812) [12,33]. The intensity of the (400) peak is higher than that of (111). However, the peak strength of (400) is less than that of (111) (Fig. 2d, red). Therefore, Sn concentration may significantly promote or inhibit crystal growth.

To elucidate the storage mechanism, we obtained the first five cyclic voltammetry (CV) curve within the range of 0.01–3.00 V

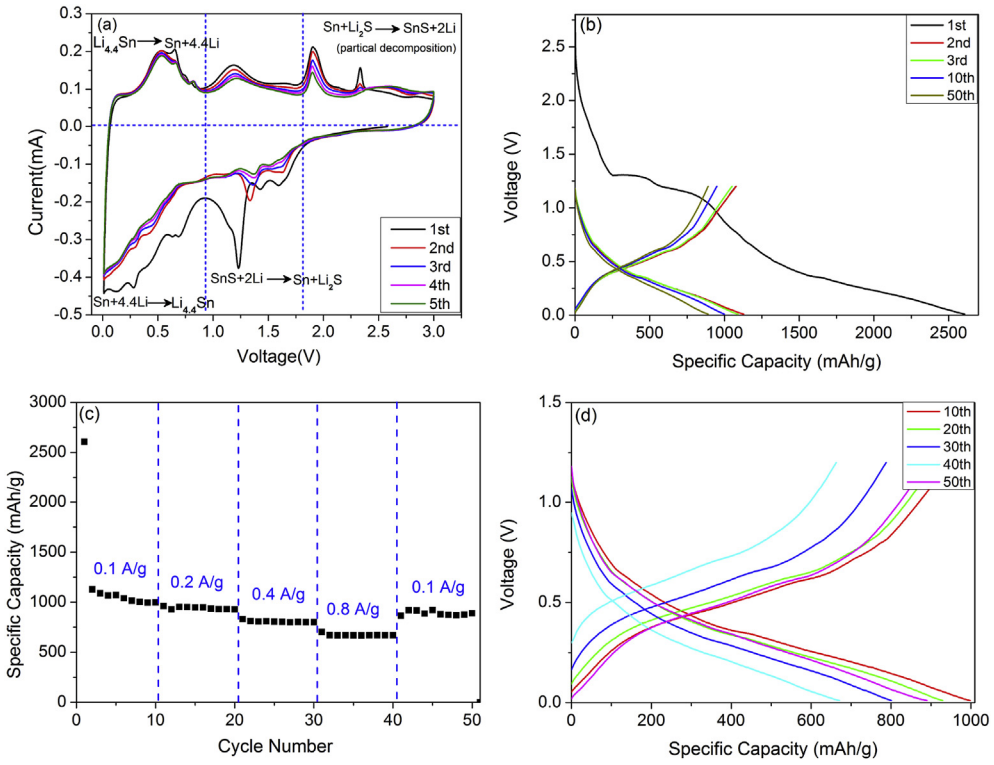

Fig. 4. (a) The five cyclic voltammograms, (b) Discharge/charge voltage profiles of SnS nanobelts anode at a current of 0.1 A/g, (c) and (d) Rate capabilities of SnS nanobelts anode; inset: discharge/charge voltage profiles of SnS nanobelts anode at current density of 0.1, 0.2, 0.4, and 0.8 A/g.

(Fig. 4a). A strong reduction peak appears at ~1.23 V and disappears in subsequent cycles, which can be attributed to the decomposition of SnS into metallic Sn and Li_2S (Eq. (1)), and the formation of irreversible solid electrolyte interphase during the first scan. The irreversible plateau appears at ~1.23 V, which corresponds to the first discharge process in the charge–discharge curves (Fig. 4b). The pair of reduction/oxidation peaks at 0.01 V/0.52 V appears in the entire cycle, and these peaks is assigned to the lithium intercalation/deintercalation reaction, as shown in Eq. (2). All peaks, in addition to the peak at ~1.23 V, repeatedly appear in the subsequent cycle curves, indicating good cycling stability of the SnS nanobelt. These findings are consistent with those in previous reports [31,33]. The oxidation peak at ~1.19 V may be attributed to the deintercalation of lithium ions from the SnS layers without phase decomposition [28]. Another two oxidation peaks at ~1.91 and ~2.32 V may be related to the Li_2S decomposition and SnS_2 reformation from the reverse of the partial conversion reaction ($Sn + Li_2S \rightarrow SnS + 2Li^+ + 2e^-$) [6,28,31]. Another two reduction peaks at ~1.42 and ~1.60 V in the subsequent cycle curves are possibly assigned to the SnS to Sn and Li_2S conversion in the reduction scan to sustain the constant rate of Li_2S decomposition during the oxidation scan, which may lead to an increase in the reversible capacity [28,30]. The theoretical capacity of SnS based on the theoretical maximum (6.4Li/Sn) is 1138 $mAhg^{-1}$ if Li_2S can be decomposed completely according to the reversible reaction ($SnS + 6.4Li^+ + 6.4e^- \leftrightarrow Li_{4.4}Sn + Li_2S$) [28–31]. The results from the redox peaks of CV plots are well matched to the galvanostatic charge/discharge cycles (Fig. 4b) of the SnS nanobelt anode that were performed within 0.1 and 1.2 V (versus Li^+/Li) at a current density of 100 mAg^{-1}.

Fig. 4b shows the initial discharge capacity of 2606.9 $mAhg^{-1}$ after the first cycle. The high discharge capacity may be attributed to the unique nanoscale structure and reactions (1, 2) between SnS and Li^+ [32]. The similar higher first discharge capacity compared with the maximum theoretical value (1138 $mAhg^{-1}$) can also be found in other reports [28,34]. The discharge capacities of 1128.5 and 1089.4 $mAhg^{-1}$ after the second and third cycles, respectively, correspond to 144% and 139% of the theoretical value of 782 $mAhg^{-1}$ (4.4Li/Sn), respectively. The discharge capacity of 1089.4 $mAhg^{-1}$ after three cycles decreases by 3% as compared to the second discharge capacity, which indicates a slight loss of capacity. The discharge capacity slightly decreases but is still high with a value of 889.9 $mAhg^{-1}$ even after 50 cycles. These values are higher than those previously reported [12,27,31]. The high discharge capacity and electrochemical performance can be attributed to the unique morphology of SnS. The SnS nanoribbons not only provide fast channels and numerous reactive sites for Li^+ diffusion (by reducing the diffusion length within the material) but also act as a buffer for volume changes during Li^+ insertion and extraction [33]. More impressively, the SnS nanobelt anode also delivers a charge capacity of 890.3 $mAhg^{-1}$ after 50 cycles by reversibly storing and retrieving 5 Li^+ per Sn atom, corresponding to the reversibility of the conversion reaction ($Sn + Li_2S \rightarrow SnS + 2Li^+ + 2e^-$) as high as 30% [28,30,35]. The decomposition and formation of Li_2S may be only partial, which may be a reason to explain the extra high capacity and excellent properties [28–30]. Fig. 4c and d reveal that the discharge capacities at the 10th cycle are 998.2, 929.4, 801.1, and 670.9 $mAhg^{-1}$ at current densities of 0.1, 0.2, 0.4, and 0.8 Ag^{-1}, respectively [26,36]. When the rate is returned back to 0.1 A/g, the discharge capacity is 889.9 $mAhg^{-1}$. The very good cycling stability and resilience of the electrode are fully indicated in such rate capability. These values are better in comparison with previous results for tin sulfide as an anode for LIBs [12,31,32,37–39] (Support information Fig. S3a).

To determine factors contributing to the excellent rate capability of the SnS electrode, we performed electrochemical impedance

spectroscopy (EIS) measurements for the fresh and spent cells by applying amplitude of 5.0 mV over the frequency range of 1000 kHz to 0.01 Hz. The impedance plots are fitted by Zsimpwin software (Fig. S3b) and consist of one depressed semicircle in the high frequency range and an inclined line in the low frequency range. The semicircles can be attributed to the internal resistance of the battery, electrolyte solution resistance, and charge transfer resistance for both electrodes [40]. The inclined lines are related to Li^+ diffusion into the bulk of the electrode material [31]. The size of semicircle for a fresh cell is lower than that after cycling, which may be associated with slight volume expansion during the process. The volume expansion may lead to slight capacity decay during circulation. The results are shown in Fig. 4c and Fig. S3c. To demonstrate the cycling stability of SnS nanobelts, we conducted TEM analysis after cycling in the presence of carbon black and PVDF binders (Fig. S3c). The nanobelt morphology is denoted by red lines, indicating that volume changes can be buffered to a certain extent.

4. Conclusions

SnS nanobelts were successfully synthesized through a universal surfactant-free and controllable hydrothermal approach without using any organic solvents. This study provides vital insights into the tunable crystal structure of SnS by controlling the mixing stages and proposes a novel formation mechanism. The SnS nanobelts display a relatively high reversible capacity of 889.9 $mAhg^{-1}$ even after 50 cycles when used as the anode of LIBS. These results may open a novel way for the synthesis of SnS nanobelts with superior cycling and rate performance for LIBs.

Acknowledgments

This work was financially supported by the National Basic Research Program of China (973 Program: 2013CB932903), the National Science Foundations of China (No. 61205057, No. 11574136), Qing Lan Project, the '1311 Talent Plan' Foundation of Nanjing University of Posts and Telecommunications, Six talent peaks project in Jiangsu Province (JY-014), the Open Research Fund of State Key Laboratory of Bioelectronics, Southeast University, and Jiangsu Provincial Key R & D Program (Grant No. BE2015700).

Appendix A. Supplementary data

Supplementary data related to this article can be found at http://dx.doi.org/10.1016/j.jallcom.2016.04.280.

References

[1] Y. Xiao, IEEE Trans. Ind. Electron. 62 (2015) 3112–3122.
[2] Y. Dong, K.C. Yung, R. Ma, X. Yang, Y.-S. Chui, J.-M. Lee, J.A. Zapien, Carbon 86 (2015) 310–317.
[3] Y. Li, S. Yu, T. Yuan, M. Yan, Y. Jiang, J. Power Sources 282 (2015) 1–8.
[4] X. Wu, S. Zhang, H. Fang, Z. Du, R. Lin, J. Power Sources 264 (2014) 311–319.
[5] X. Xu, C. Takai, T. Shirai, M. Fuji, Adv. Powder Technol. 26 (2015) 1327–1334.
[6] S.H. Choi, Y.C. Kang, Nano Res. 8 (2015) 1595–1603.
[7] T.-J. Kim, C. Kirn, D. Son, M. Choi, B. Park, J. Power Sources 167 (2007) 529–535.
[8] Y. Zou, Y. Wang, Chem. Eng. J. 229 (2013) 183–189.
[9] B. Wang, W. Al Abdulla, D. Wang, X.S. Zhao, Energy & Environ. Sci. 8 (2015) 869–875.
[10] S.R. Suryawanshi, S.S. Warule, S.S. Patil, K.R. Patil, M.A. More, ACS Appl. Mater. Interfaces 6 (2014) 2018–2025.
[11] J. Chao, Z. Wang, X. Xu, Q. Xiang, W. Song, G. Chen, J. Hu, D. Chen, RSC Adv. 3 (2013) 2746–2753.
[12] D.D. Vaughn II, O.D. Hentz, S. Chen, D. Wang, R.E. Schaak, Chem. Commun. 48 (2012) 5608–5610.
[13] A.M. Tripathi, S. Mitra, RSC Adv. 4 (2014) 10358–10366.
[14] S.R. Suryawanshi, S.S. Warule, S.S. Patil, K.R. Patil, M.A. More, ACS Appl. Mater. Interfaces 6 (2014) 2018–2025.
[15] H.S. Im, Y. Myung, Y.J. Cho, C.H. Kim, H.S. Kim, S.H. Back, C.S. Jung, D.M. Jang, Y.R. Lim, J. Park, J.-P. Ahn, RSC Adv. 3 (2013) 10349–10354.
[16] S. Hori, T. Suzuki, T. Suzuki, T. Suzuki, S. Nonomura, Jpn. J. Appl. Phys. 53 (2014).
[17] X. Liu, Y. Li, B. Zhou, X. Wang, A.N. Cartwright, M.T. Swihart, Chem. Mater. 26 (2014) 3515–3521.
[18] Z. Deng, D. Cao, J. He, S. Lin, S.M. Lindsay, Y. Liu, ACS Nano 6 (2012) 6197–6207.
[19] A.J. Biacchi, D.D. Vaughn II, R.E. Schaak, J. Am. Chem. Soc. 135 (2013) 11634–11644.
[20] X. Zhang, L. Yang, Y. Jiang, B.-B. Yu, Y.-G. Zou, Y. Fang, J.-S. Hu, L.-J. Wan, Chem. Asian J. 8 (2013) 2483–2488.
[21] B. Wang, A. Liu, W. Al Abdulla, D. Wang, X.S. Zhao, Nanoscale 7 (2015) 8819–8828.
[22] H. Zhang, B.-R. Hyun, F.W. Wise, R.D. Robinson, Nano Lett. 12 (2012) 5856–5860.
[23] J.-G. Kang, Y.-D. Ko, K.J. Choi, J.-G. Park, D.-W. Kim, Appl. Phys. Mater. Sci. Process. 103 (2011) 505–510.
[24] S. Li, J. Zheng, Z. Hu, S. Zuo, Z. Wu, P. Yan, F. Pan, RSC Adv. 5 (2015) 72857–72862.
[25] L. Mei, C. Xu, T. Yang, J. Ma, L. Chen, Q. Li, T. Wang, J. Mater. Chem. A 1 (2013) 8658–8664.
[26] H.S. Im, Y.J. Cho, Y.R. Lim, C.S. Jung, D.M. Jang, J. Park, F. Shojaei, H.S. Kang, ACS Nano 7 (2013) 11103–11111.
[27] J.-G. Kang, J.-G. Park, D.-W. Kim, Electrochem. Commun. 12 (2010) 307–310.
[28] A.M. Tripathi, S. Mitra, RSC Adv. 5 (2015) 23671–23682.
[29] S. Liu, X. Lu, J. Xie, G. Cao, T. Zhu, X. Zhao, ACS Appl. Mater. Interfaces 5 (2013) 1588–1595.
[30] B. Qu, G. Ji, B. Ding, M. Lu, W. Chen, J.Y. Lee, Chemelectrochem 2 (2015) 1138–1143.
[31] M. Zhang, D. Lei, X. Yu, L. Chen, Q. Li, Y. Wang, T. Wang, G. Cao, J. Mater. Chem. 22 (2012) 23091–23097.
[32] J. Lu, C. Nan, L. Li, Q. Peng, Y. Li, Nano Res. 6 (2013) 55–64.
[33] T. Zhou, W.K. Pang, C. Zhang, J. Yang, Z. Chen, H.K. Liu, Z. Guo, ACS Nano 8 (2014) 8323–8333.
[34] Z. Fang, Q. Wang, X. Wang, F. Fan, C. Wang, X. Zhang, Mater. Res. Bull. 48 (2013) 4935–4941.
[35] H. Chauhan, M.K. Singh, S.A. Hashmi, S. Deka, RSC Adv. 5 (2015) 17228–17235.
[36] R. Chen, T. Zhao, W. Wu, F. Wu, L. Li, J. Qian, R. Xu, H. Wu, H.M. Albishri, A.S. Al-Bogami, D. Abd El-Hady, J. Lu, K. Amine, Nano Lett. 14 (2014) 5899–5904.
[37] J. Cai, Z. Li, P.K. Shen, ACS Appl. Mater. Interfaces 4 (2012) 4093–4098.
[38] S. Li, S. Zuo, Z. Wu, Y. Liu, R. Zhuo, J. Feng, D. Yan, J. Wang, P. Yan, Electrochim. Acta 136 (2014) 355–362.
[39] G.G. Kumar, K. Reddy, K.S. Nahm, N. Angulakshmi, A.M. Stephan, J. Phys. Chem. Solids 73 (2012) 1187–1190.
[40] S. Li, J. Zheng, S. Zuo, Z. Wu, P. Yan, F. Pan, RSC Adv. 5 (2015) 46941–46946.